View metadata, citation and similar papers at core.ac.uk
brought to you by CORE
provided by Digital Repository @ Iowa State University

ULTRASONIC MODELING OF REAL-LIFE NDT SITUATIONS:

APPLICATIONS AND FURTHER DEVELOPMENTS

R. Marklein, K. J. Langenberg, S. Klaholz, J. Kostka
Department of Electrical Engineering
University of Kassel
D-34109 Kassel, Germany

INTRODUCTION

In order to cope with real-life NDT situations, we have to develop numerical time domain modeling tools which are based on direct numerical methods because only very few idealized canonical NDT situations can be modeled with analytical methods. Well known direct numerical procedures for the time domain modeling of ultrasonic waves (elastodynamic waves) are given in the references [1]-[6]. One of these, the Elastodynamic Finite Integration Technique (EFIT) [6, 7], has been applied to several real-life NDT situations. A subset of six 2D EFIT simulations include the NDT of a welded high pressure vessel, ultrasonic pipeline inspection, NDT of concrete (NDT-CE) (the reader is referred to [8]), NDT of fiber reinforced laminates, NDT of fiber reinforced T-stringer, and transducer modeling.

NDT OF A WELDED HIGH PRESSURE VESSEL

The first modeling example is the NDT of a welded high pressure vessel. Fig. 1.a shows the geometry with the size of 300mm×192mm. The material parameters are $c_{\mathrm{P}}^{\mathrm{steel}}$=5960 m/s, $c_{\mathrm{S}}^{\mathrm{steel}}$=3260 m/s and $\varrho_0^{\mathrm{steel}}$=7870 kg/m^3. We presume a crack with a depth of d=5mm in the right side of the weld. The weld itself is modeled by the same steel and is indicated by the dashed lines. We applied a 45° shear wave probe MWB45-2 which has a center frequency of 2 MHz. A spatial discretization with $\Delta x = 100\mu$m yields a mesh size of MS=1,500×960=1,440,000 material cells. A snapshot of the magnitude of the particle velocity vector $\underline{\mathbf{v}}$ is overlayed in Fig. 1.a which shows the radiated ultrasonic wavefield. We „recorded“ (modeled) 84 A-scans in pulse-echo mode within a synthetic aperture which is indicated by the black bar (see Fig. 1.a). We applied a SAFT imaging algorithm to the rf-data field. The reconstructed image is shown in Fig. 1.b. The image gives a clear indication for the backwall-breaking crack. But, for this small crack depth of 5mm we are unable to determine the real depth from the SAFT image with a 2 MHz probe. This has been also proved for experimental data.

ULTRASONIC PIPELINE INSPECTION

We modeled several NDT situations: We varied the insonification angle α for one crack configuration and we varied the crack position x from the insonification point E for one selected insonification angle α. Essentially, we studied two different

Review of Progress in Quantitative Nondestructive Evaluation, Vol. 15
Edited by D.O. Thompson and D.E. Chimenti, Plenum Press, New York, 1996

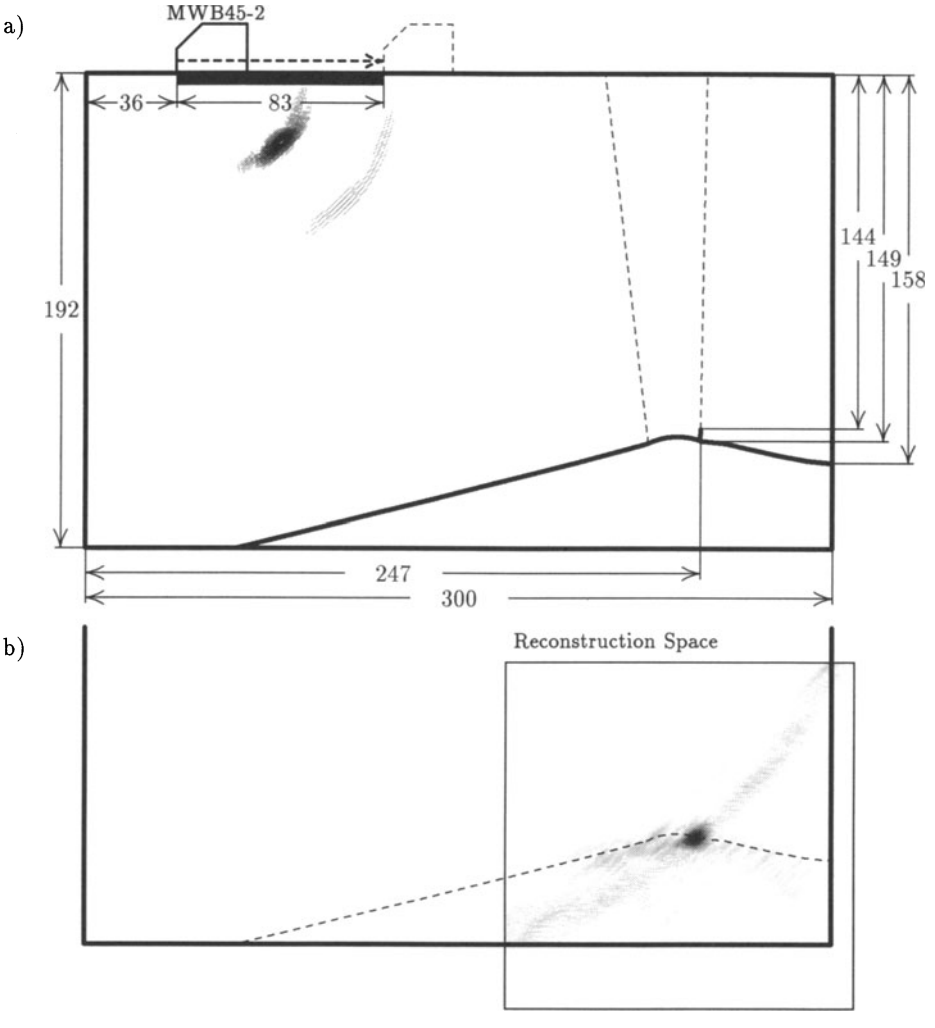

Figure 1. a) Geometry of the welded high pressure vessel and 2D EFIT-$|\underline{\mathbf{v}}|$-snapshot of the ultrasonic wavefield excited by a MWB45-2 probe; b) SAFT imaging as applied to a rf-data field modeled with the 2D EFIT code.

crack situations: (1) cracks in the water/steel interface (interface or internal cracks) and (2) backwall-breaking cracks (external cracks). The parameters of the materials used are $c_{\mathrm{P}}^{\mathrm{steel}}$=5960 m/s, $c_{\mathrm{S}}^{\mathrm{steel}}$=3225 m/s, $\varrho_0^{\mathrm{steel}}$=7700 kg/m^3 and $c_{\mathrm{P}}^{\mathrm{water}}$=1483 m/s, $\varrho_0^{\mathrm{water}}$=998 kg/m^3. The geometry for 2D EFIT modeling is given in Fig. 2, here with an interface crack at x=40mm. Fig. 3 shows two EFIT-$|\underline{\mathbf{v}}|$-snapshots for an insonification angle of α=18°. The modeled A-scan is displayed at the top of Fig. 4. Below that a comparison between the modeled ALOK-scan with the corresponding experimental ALOK-scan is given. We find convincing coincidence. The 4 strongest echos are interpreted by the EFIT-$|\underline{\mathbf{v}}|$-snapshots.

EFIT-4S2T: EFIT 4th Order in Space and 2nd Order in Time

If we compare both EFIT-$|\underline{\mathbf{v}}|$-snapshots in Fig. 3, we clearly recognize that the pulse width in water increases with the computed time steps. This unphysical

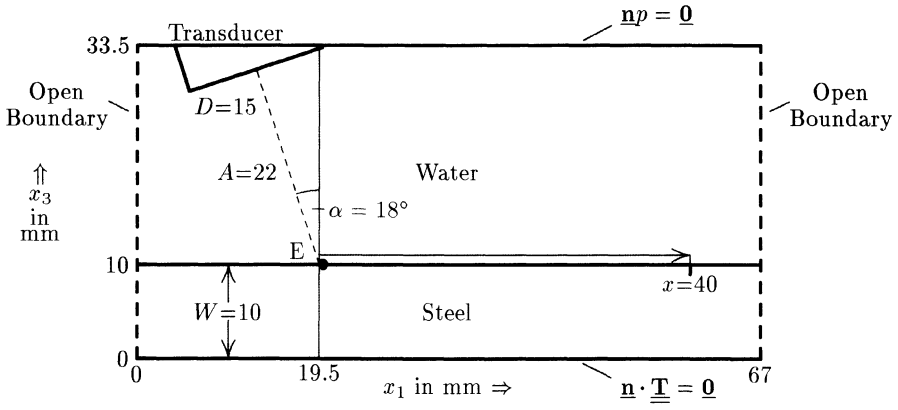

Figure 2. Ultrasonic pipeline inspection: geometry for 2D EFIT modeling.

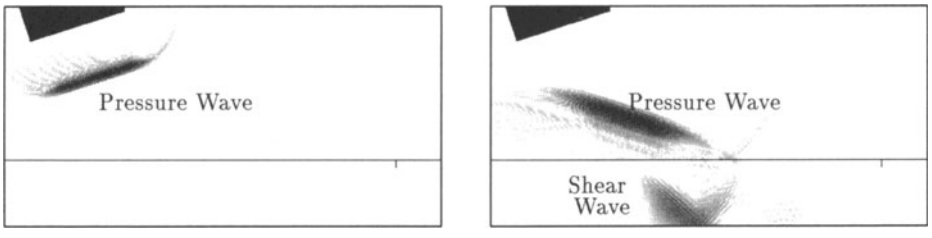

Figure 3. EFIT-$|\underline{v}|$-snapshots of the ultrasonic wave field.

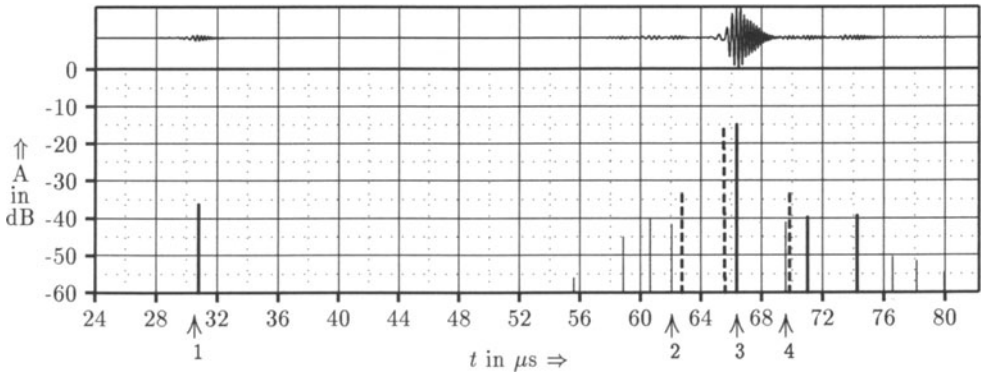

Figure 4. Top: modeled A-scan; bottom: comparison between modeled (solid line) and experimental ALOK-scan (dashed line). 1: P-P; 2: P-4S-2S-P; 3: P-4S-4S-P; 4: P-4S-6S-P.

dispersion is a known problem in hyperbolic solvers and it is due to numerical dispersion which is defined through the (numerical) dispersion equation [6, 9]. Until now, we apply an EFIT code which is 2nd order in space and time (EFIT-2S2T). In order to tackle this problem, we recently developed EFIT code (EFIT-4S2T) which is 4th order in space and 2nd order in time. (But this code can currently be applied only to isotropic problems.) With the application of the EFIT-4S2T code numerical

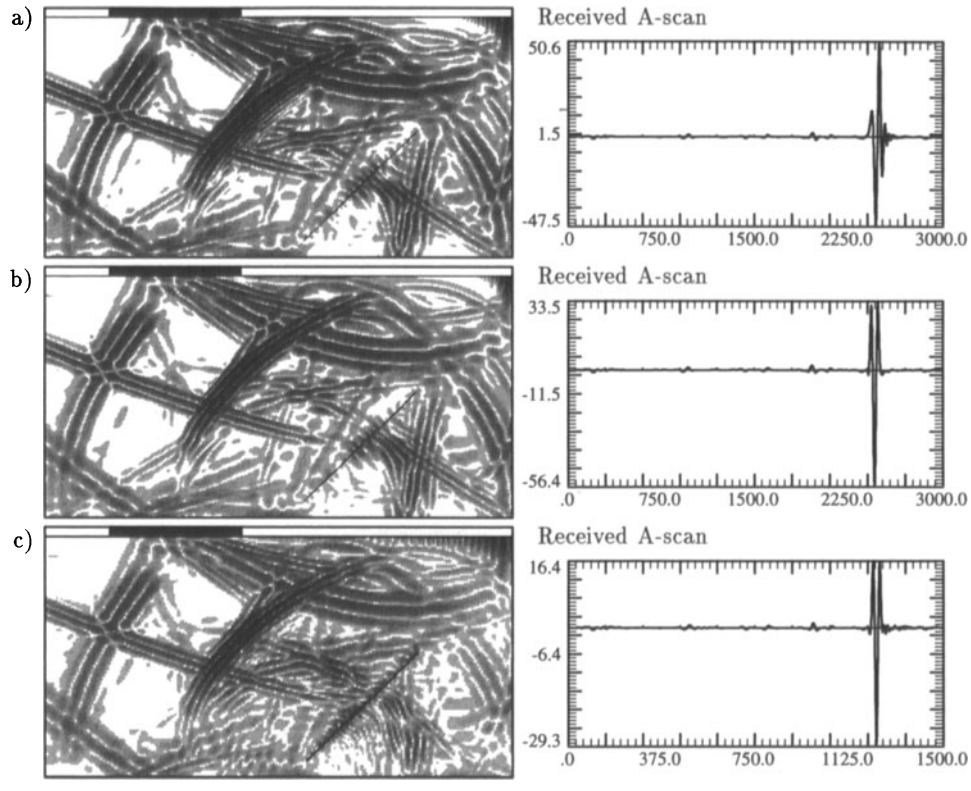

Figure 5. a) EFIT-2S2T (mesh size 1005×270, Δx=100μm); b) EFIT-4S2T (mesh size 1005×270, Δx=100μm); c) EFIT-4S2T (reduced mesh size 502×135, Δx=200μm).

dispersion is reduced. The discrete equation for the EFIT-2S2T-v_1-component reads

$$\begin{aligned}\dot{v}_1^{(i_1+\frac{1}{2},i_2,i_3)}(t) = \frac{1}{\varrho_0{}^{(i_1+\frac{1}{2},i_2,i_3)}} \Bigg\{ & \frac{1}{\Delta x_1}[T_{11}^{(i_1+1,i_2,i_3)}(t) - T_{11}^{(i_1,i_2,i_3)}(t)] \\ & + \frac{1}{\Delta x_2}[T_{12}^{(i_1+\frac{1}{2},i_2+\frac{1}{2},i_3)}(t) - T_{12}^{(i_1+\frac{1}{2},i_2-\frac{1}{2},i_3)}(t)] \\ & + \frac{1}{\Delta x_3}[T_{13}^{(i_1+\frac{1}{2},i_2,i_3+\frac{1}{2})}(t) - T_{13}^{(i_1+\frac{1}{2},i_2,i_3-\frac{1}{2})}(t)] + f_1^{(i_1+\frac{1}{2},i_2,i_3)} \Bigg\} \end{aligned} \tag{1}$$

and for EFIT-4S2T we have now

$$\begin{aligned}\dot{v}_1^{(i_1+\frac{1}{2},i_2,i_3)}(t) = \frac{1}{\varrho_0{}^{(i_1+\frac{1}{2},i_2,i_3)}} \Bigg\{ & \frac{1}{\Delta x_1}[T_{11}^{(i_1+1,i_2,i_3)}(t) - T_{11}^{(i_1,i_2,i_3)}(t)] \\ & - \frac{1}{24\Delta x_1}[T_{11}^{(i_1+2,i_2,i_3)}(t) - 3T_{11}^{(i_1+1,i_2,i_3)}(t) + 3T_{11}^{(i_1,i_2,i_3)}(t) - T_{11}^{(i_1-1,i_2,i_3)}(t)] \\ & + \frac{1}{\Delta x_2}[T_{12}^{(i_1+\frac{1}{2},i_2+\frac{1}{2},i_3)}(t) - T_{12}^{(i_1+\frac{1}{2},i_2-\frac{1}{2},i_3)}(t)] \\ & - \frac{1}{24\Delta x_2}[T_{12}^{(i_1+\frac{1}{2},i_2+\frac{3}{2},i_3)}(t) - 3T_{12}^{(i_1+\frac{1}{2},i_2+\frac{1}{2},i_3)} + 3T_{12}^{(i_1+\frac{1}{2},i_2-\frac{1}{2},i_3)}(t) - T_{12}^{(i_1+\frac{1}{2},i_2-\frac{3}{2},i_3)}(t)] \\ & + \frac{1}{\Delta x_3}[T_{13}^{(i_1+\frac{1}{2},i_2,i_3+\frac{1}{2})}(t) - T_{13}^{(i_1+\frac{1}{2},i_2,i_3-\frac{1}{2})}(t)] \end{aligned}$$

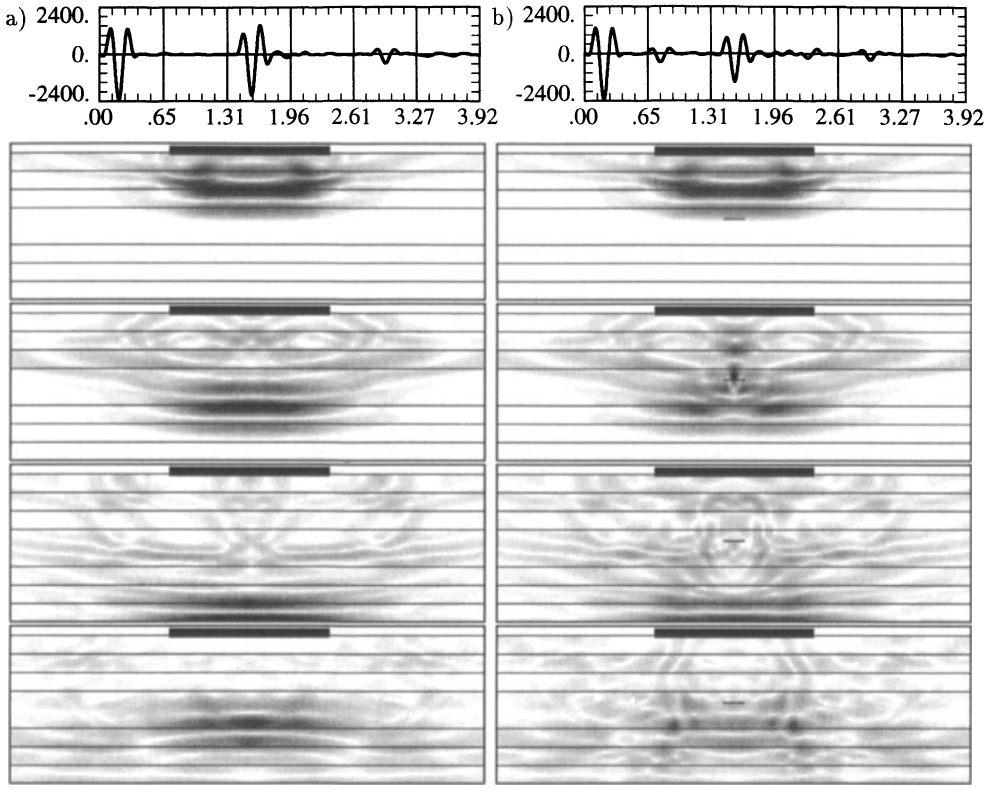

Figure 6. EFIT-$|\underline{\mathbf{v}}|$-snapshots: a) cross laminate and b) cross laminate with a delamination of $250\mu\text{m}\times12.5\mu\text{m}$.

$$-\frac{1}{24\Delta x_3}[\mathrm{T}_{13}^{(i_1+\frac{1}{2},i_2,i_3+\frac{3}{2})}(t) - 3\mathrm{T}_{13}^{(i_1+\frac{1}{2},i_2,i_3+\frac{1}{2})}(t) + 3\mathrm{T}_{13}^{(i_1+\frac{1}{2},i_2,i_3-\frac{1}{2})}(t) - \mathrm{T}_{13}^{(i_1+\frac{1}{2},i_2,i_3-\frac{3}{2})}(t)]$$
$$+ f_1^{(i_1+\frac{1}{2},i_2,i_3)}\Big\} \; ; \qquad (2)$$

T_{1i}, $i = 1,\ldots 3$ are the stress tensor components and f_1 is the first component of the body volume force vector. Fig. 5 gives a first comparison between 2D EFIT-2S2T and 2D EFIT-4S2T for the 45° shear wave scattering by a 45° tilted crack. The probe is a 45° shear wave probe MWB45-2 with a RC2 time history. First we modeled this situation with the EFIT-2S2T code. The mesh size is 1005×270 with a Δx=100μm and we computed 3000 time steps. Results are given in Fig. 5.a. The A-scan documents the numerical dispersion for the EFIT-2S2T code. Then, we modeled the same situation with the EFIT-4S2T code. Fig. 5.b shows the snapshot and received A-scan which has „no" significant dispersion anymore through eyeball comparison. Finally, we reduced the mesh size and the number of time steps to Δx=200μm and NT=1500 in order to save main memory and computational time. The results of the EFIT-4S2T code are shown in Fig. 5.c which are still more accurate in the sense of numerical dispersion than the EFIT-2S2T results (Fig. 5.a). All these effects can be explained theoretically.

NDT OF FIBER REINFORCED COMPOSITES

Here we modeled the ultrasonic wave propagation and scattering in several anisotropic composite configurations. Fig. 6 shows EFIT results of ultrasonic waves in

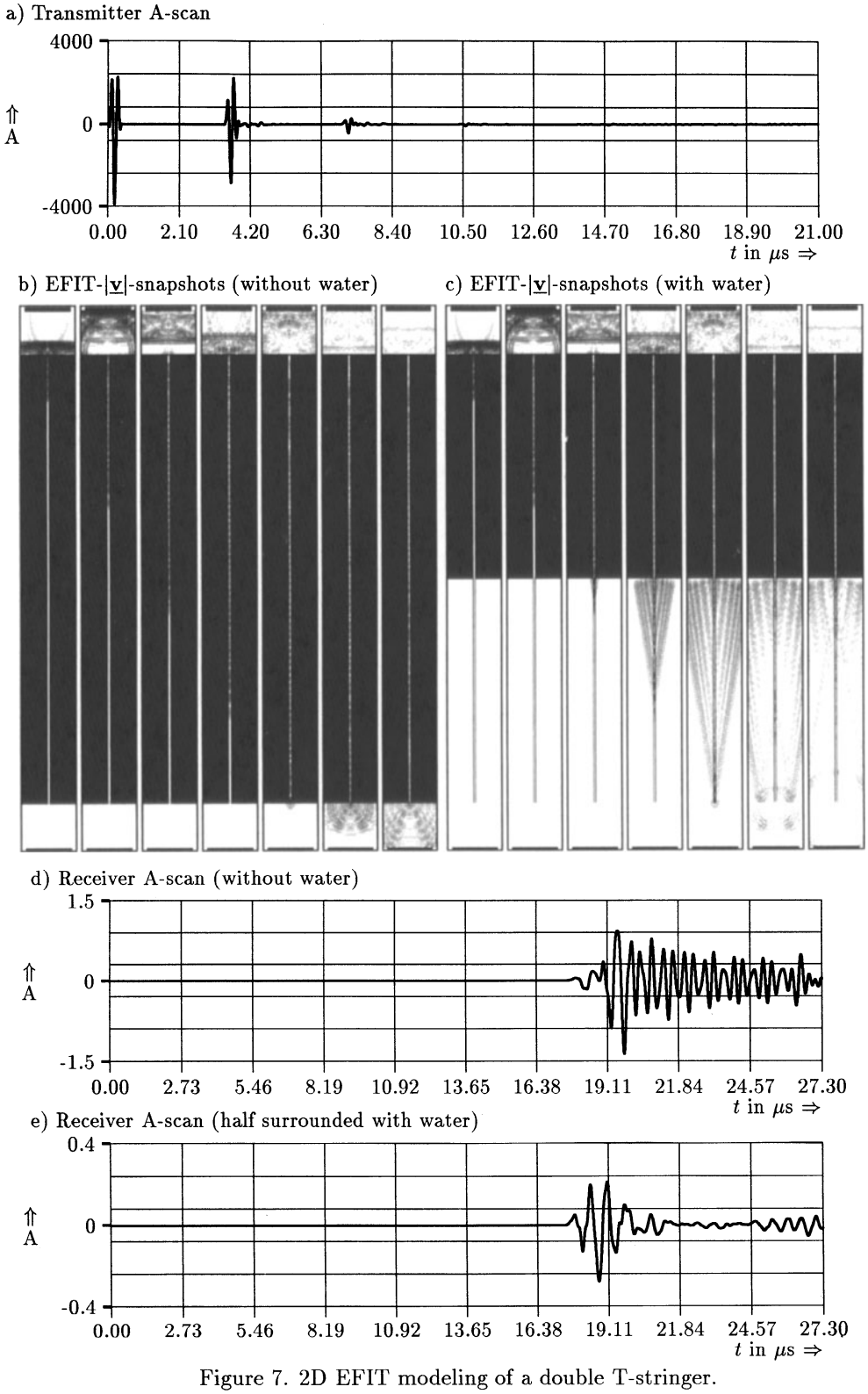

Figure 7. 2D EFIT modeling of a double T-stringer.

a graphite epoxy cross laminate of the size 6mm×2mm with 16 layers. The fiber direction rotates in the xy-plane from top to bottom according to α_{xy}={ 0°, 0° 90°, 90° 0°, 0° 90°, 90° 90°, 90° 0°, 0° 90°, 90° 0°, 0° } degree around the vertical axis (z-axis). We investigated the influence of the anisotropy on the received signal for a normal pressure probe. Furthermore, we modeled the crack scattering by surface parallel delaminations of different sizes. Fig. 6.a shows EFIT-$|\underline{\mathbf{v}}|$-snapshots of the transducer radiation and at the top a modeled A-scan of a 5 MHz normal pressure probe. In order to take into account the energy absorption mechanism of the probe we applied an absorbing boundary condition (ABC) at the probe sole. Fig. 6.b displays the crack scattering on a delamination of width w =250μm and a thickness of t=Δx=12.5μm.

NDT OF FIBER REINFORCED DOUBLE T-STRINGER

In the construction of aircraft wings fiber reinforced graphite epoxy material is a new-fangled material. This material has a transverse isotropy characterized by the fiber direction $\underline{\hat{\mathbf{m}}}$. For example, an aircraft wing consists of multiple double T-stringers which are made of fiber reinforced composites and which are built up in a honeycomb structure. At the I-section interface the double T-stringer has a very complicated variation of the fiber direction. In our used model for numerical EFIT modeling we presume a perpendicular fiber direction at this intersection. Therefore, in the upper and lower part we have a horizontal and in the I-section a vertical fiber direction. Selected EFIT-$|\underline{\mathbf{v}}|$-snapshots of the elastic wavefield of a 5 MHz normal pressure probe are given in Fig. 7.b. At the sole of the transmitter and receiver we applied an absorbing boundary condition (ABC) in order to take into account the energy absorption of the mounted probe. The transmitter signal is shown in Fig. 7.a. The time history of the probe is modeled by a RC2 pulse. The receiver signal is displayed in Fig. 7.d. This signal represents an echo sequence which is due to the wave guide behavior of the I-section. In a second EFIT modeling we half surrounded the I-section with water in order to model a half filled tank. Fig. 7.c shows the according EFIT-$|\underline{\mathbf{v}}|$-snapshots. Obviously, when the Lamb wave arrives at the water/I-section interface Leaky waves appear. Further, when the Lamb wave hits the lower corners of the I-section Scholte waves are generated which are traveling up along the water/I-section interface. The received signal is given in Fig. 7.e. Because of the leackage effect the amplitude of the received echo decreases and the wave guiding effect appears weaker. Due to this we received only one single transmitted echo and not a whole echo sequence as in Fig. 7.d.

TRANSDUCER MODELING

We modeled several transducers in order to calculate the radiation pattern for different isotropic or anisotropic solid materials. The left side of Fig. 8 shows the 2D EFIT modeling of the radiation of a MWB45-2 probe into isotropic aluminum in comparison to the radiation of the same probe into transversely isotropic austenite with a horizontal fiber direction. For each case we calculated a „broadband“ radiation pattern of the displayed EFIT-$|\underline{\mathbf{v}}|$-snapshot. For the isotropic aluminum the desired angle of 45° degree is observed. But for the transversely isotropic austenite the main lobe has an angle of ca. 87.5° degree. This effect is due to the anisotropy of austenite which is already studied elsewhere [6, 7].

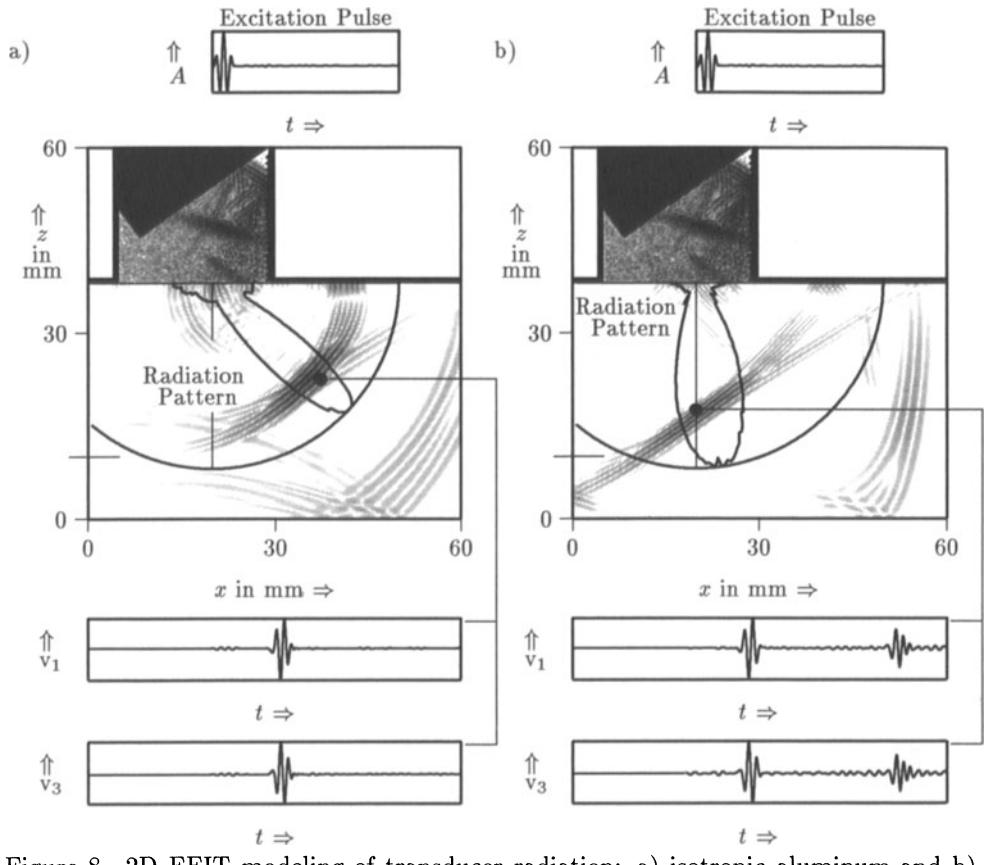

Figure 8. 2D EFIT modeling of transducer radiation: a) isotropic aluminum and b) transversely isotropic austenite with a horizontal fiber direction ($\underline{\hat{\mathbf{m}}} = \underline{\mathbf{e}}_x$).

REFERENCES

1. Z. S. Alterman, J. Phys. Earth, **16** (1968)
2. L. J. Bond, in: Research Techniques in NDT, **6**, eds.: R. S. Sharpe, Academic Press, London (1982) pp. 107-150
3. P. Madariaga, Bull. Seis. Soc. of Am., **66**, 3 (1976) pp. 639-666
4. J. Virieux, Geophysics, **51**, 4 (1986) pp. 889-901
5. R. Ludwig, W. Lord, IEEE Trans. Ultrasonics, Ferroelectrics, and Frequency Control, **35**, 6 (1988) pp. 809-820
6. P. Fellinger, R. Marklein, K. J. Langenberg, S. Klaholz, Wave Motion **21** (1995) pp. 47-66
7. R. Marklein, R. Bärmann, K. J. Langenberg, in: Review of Progress in Quantitative Nondestructive Evaluation 1994, eds.: D. O. Thompson, D. E. Chimenti, **14**, Plenum Press, New York (1995) pp. 251-258
8. R. Marklein, K. J. Langenberg, R. Bärmann, M. Brandfaß, these proceedings
9. R. Marklein, Master Thesis, Kassel (1992)